Faster high-speed atomic force microscopy for imaging of biomolecular processes

Shingo Fukuda, and Toshio Ando

View Online   Export Citation   CrossMark
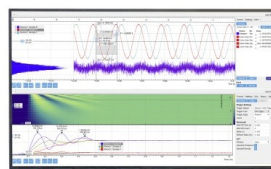
Faster high-speed atomic force microscopy for imaging of biomolecular processes

View Online   Export Citation   CrossMark

Shingo Fukuda (ID) **and Toshio Ando**[a] (ID)

AFFILIATIONS

Nano Life Science Institute (WPI-NanoLSI), Kanazawa University, Kakuma-machi, Kanazawa 920-1192, Japan

[a]**Author to whom correspondence should be addressed:** tando@staff.kanazawa-u.ac.jp

ABSTRACT

High-speed atomic force microscopy (HS-AFM) has enabled observing protein molecules during their functional activity at rates of 1–12.5 frames per second (fps), depending on the imaging conditions, sample height, and fragility. To meet the increasing demand for the great expansion of observable dynamic molecular processes, faster HS-AFM with less disturbance is imperatively needed. However, even a 50% improvement in the speed performance imposes tremendous challenges, as the optimization of major rate-limiting components for their fast response is nearly matured. This paper proposes an alternative method that can lower the feedback control error and thereby enhance the imaging rate. This method can be implemented in any HS-AFM system by minor modifications of the software and hardware. The resulting faster and less-disturbing imaging capabilities are demonstrated by the imaging of relatively fragile actin filaments and microtubules near the video rate, and of actin polymerization that occurs through weak intermolecular interactions, at ~8 fps.

I. INTRODUCTION

High-speed atomic force microscopy (HS-AFM) operating in the amplitude-modulation (AM) mode was established in 2008 through the development of various components and control techniques,[1] such as small cantilevers,[2,4] optical beam deflection detectors optimized for small cantilevers,[3,5] fast deflection-to-amplitude converters,[1,2] fast scanners,[6,7] active vibration damping techniques,[8] and dynamic feedback controllers capable of automatic gain tuning during imaging.[9] In the AM mode, the cantilever oscillation amplitude is maintained at its set point value by feedback Z-scanning of the sample stage (or the cantilever chip). The feedback control error increases with increasing X-scan velocity. In particular, the error becomes large in the step height (edge) regions. When the error exceeds a certain level depending on the sample fragility, the tip–sample contact disturbs the biological function of the sample and can even destroy the sample. Several strategies have been employed to minimize disturbance to a sample. For filamentous protein assemblies, filaments oriented approximately along the fast X-scanning direction have been adopted for imaging. This orientation minimizes step height changes, thereby reducing both the tip–sample contact strength and tip parachuting (i.e., complete loss of tip–sample contact), as exemplified in the imaging of

myosin V walking on actin filaments at 7 frames per second (fps).[10] Meanwhile, the surface density of globular proteins on a substrate has been increased to narrow their inter-molecular gaps, producing a smaller step height, as demonstrated by the imaging of double-ring GroEL of height ~15 nm interacting with its co-chaperonin GroES at 1–2 fps.[6,11] Alternatively, the lateral scan size can be minimized to reduce the X-scan velocity, allowing an increased imaging rate, as illustrated by the imaging of F_1-ATPase lacking the γ-subunit at 12.5 fps.[12] Moreover, when a molecular process proceeds through a second-order reaction, the concentration of species involved in the reaction is lowered for slower dynamics, allowing for slower and hence less disturbing imaging. This strategy has been used in the imaging of conformational changes of ATPases[6,10–13] and self-assembly processes.[14–16] By adapting these means to an end (when necessary and possible), HS-AFM has been successfully used to visualize various protein molecules in dynamic action at 1–12.5 fps (see Refs. 17–20 and references therein).

Although the highest possible imaging rate of HS-AFM in the AM-mode depends on the imaging conditions, such as the scan range and number of scan lines, major imaging-rate determinants are the feedback bandwidth of the HS-AFM system, including the cantilever, as well as the sample fragility and height.[21] It is possible to image at > 30 fps low-height samples, such as membrane-embedded

membrane proteins with small protrusions (<~1 nm) from the membrane surface[22] and highly disordered, intrinsically disordered proteins with diameters of ~0.15 nm,[23] and robust molecules, such as dsDNA. However, most proteins do not meet these conditions. Moreover, many biomolecular processes occur in a shorter time scale (<0.1 s) and/or through weak intermolecular interactions. In particular, protein self-assembly processes often occur through weak intermolecular interactions; imaging them with HS-AFM is infeasible, as demonstrated in a study of the centriolar scaffold protein SAS-6.[24] Therefore, there is a growing need for further improvement toward faster and less disturbing imaging capabilities. Even after the establishment of HS-AFM, several efforts have been made to optimize components (except cantilevers) for a faster response.[25–27] Nonetheless, even a 50% increase in the imaging rate has been difficult because the cantilever resonant frequency has become the dominant determinant of the feedback bandwidth. Furthermore, it is difficult to fabricate smaller cantilevers with a resonant frequency higher than ~1.5 MHz in water and a small spring constant (~0.1 N/m).

In this study, we explored an alternative approach to achieve a faster and less disturbing performance. Based on our observation that retrace imaging during backward x-scanning produces larger feedback error than trace imaging, we eliminated retrace imaging and shortened the time of backward scanning. This elimination and the time reduction could be carried out by simple modifications of the hardware and software of our HS-AFM system. This method can be easily implemented in any HS-AFM system.

II. RESULTS AND DISCUSSIONS

A. Feedback error comparison between trace and retrace scanning processes

In AFM imaging, the sample stage (or the cantilever chip) is generally raster scanned; along the fast scan X axis, the sample is traced and retraced with the tip in the forward and backward directions, respectively. The X axis is set parallel to the longitudinal axis of the projection of the cantilever beam onto the substrate surface. This arrangement can avoid twisting of the cantilever beam around its longitudinal axis. Assuming that the tip is attached to the left end of the cantilever beam, trace imaging is generally carried out from left to right of the sample, whereas retrace imaging is carried out from right to left [see Fig. 1(a)]. Because images acquired in the trace and retrace scanning processes are almost identical in the AM mode, as well as in other AC modes, only images acquired during trace scanning are generally recorded. However, the similarity between the trace and retrace images has only been checked using slow AFM. In this study, we first examined this issue using HS-AFM. We used relatively fragile actin filaments and microtubules (MTs) as the test samples. The former were bound to phalloidin and the latter to taxol, unless stated otherwise. These chemicals prevent depolymerization of the respective polymers upon dilution for HS-AFM imaging.

To evaluate the feedback control error, we first imaged a glutaraldehyde-treated actin filament (height $h_0 \approx 8$ nm) attached onto an amino-silane-coated mica surface [Fig. 1(b)] using a short cantilever (AC10DS, Olympus) with an electron beam deposited (EBD) tip of ~0.7 μm in length grown on the original tip of ~2 μm.
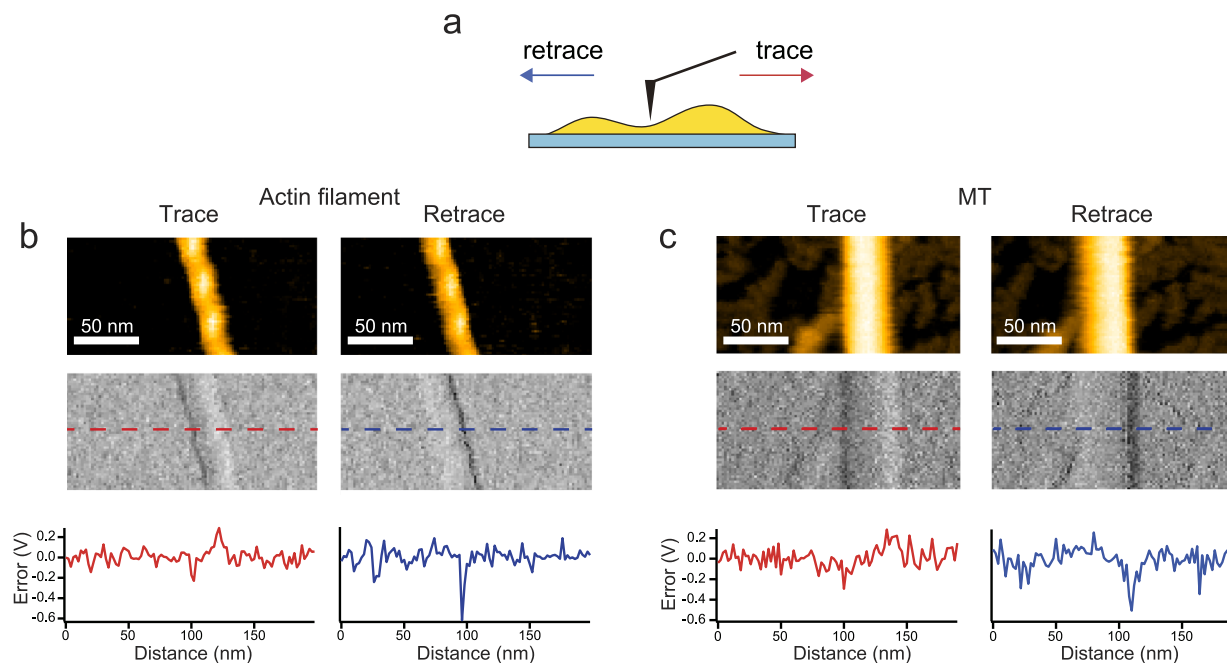
FIG. 1. Difference in feedback control error between the trace and retrace scanning processes. (a) Schematic of the trace and retrace scanning processes. [(b) and (c)] Topography (top) and error (middle) images of the actin filament (b) and MT (c) captured at 5 fps during trace and retrace scanning processes. The graphs (bottom) represent the error signal profiles measured along the broken lines shown in the error images.

This cantilever (length: 10 μm and width: 2 μm) has a spring constant $k_c \approx 0.1$ N/m, resonant frequency $f_c \approx 500$ kHz in water, and quality factor $Q_c \approx 1.5$ in water. In this imaging at 5 fps, we chose an actin filament oriented nearly along the Y axis. This orientation produces a relatively large feedback error in the positive and negative step height regions of the sample. The imaging parameters were set as follows: X-scan velocity $V_x = 110$ μm/s, scan area = 200×100 nm^2, cantilever free oscillation amplitude $A_f = 2.25$ nm, and cantilever set point amplitude $A_s = 0.85 \times A_f$. The trace and retrace topography images appeared similar [Fig. 1(b), top]. However, the error images obtained during the trace (forward) and retrace (backward) scanning processes [Fig. 1(b), middle] differ remarkably in the positive step height regions. Specifically, the right edge of the actin filament appeared darker in the error image acquired during backward scanning, compared with its left counterpart acquired during forward scanning. Note that we took the error signal ε as $\varepsilon = (A - A_s)$, where A represents the cantilever oscillation amplitude measured during imaging. Therefore, pixels in the error image appear darker when $A < A_s$ and brighter when $A > A_s$. The error signal profiles along the X axis clearly indicated a large error difference between the trace and retrace scanning processes [Fig. 1(b), bottom]. Note that the error in the negative step height region diminished rapidly. This is because our system is equipped with a dynamic feedback controller that can suppress tip parachuting at a negative step height. The peak error at the positive step height (-0.6 V) in the retrace image corresponds to $\varepsilon = -0.9$ nm based on the amplitude detection sensitivity of 1.5 nm/V. In contrast, in the trace image, the peak error at the positive step height is -0.2 V, corresponding to $\varepsilon = -0.3$ nm. We confirmed a similar error signal difference between the trace and retrace scanning processes by imaging a glutaraldehyde-treated MT of larger height ($h_0 \approx 25$ nm) using the same imaging conditions as those for the actin filament [Fig. 1(c)]. Remarkably, the errors in the trace and retrace images detected in the respective positive step height regions were, however, almost identical to those observed for the actin filament [Figs. 1(b) and 1(c), bottom]. We will discuss later this error similarity between the two samples.

What does create the error difference between the trace and retrace scanning processes? Under the conditions used above ($V_x = 110$ μm/s and $f_c = 500$ kHz), the X-scanner is displaced by 0.22 nm during a single cycle of cantilever oscillation. The peak-to-peak free oscillation amplitude ($2 \times A_f = 4.5$ nm) is less than the heights of an actin filament and an MT. Therefore, during imaging of their steep positive step height regions, the tip can be laterally pushed from the sample by ~0.1–0.2 nm during a single cycle of oscillation. Although this distance is not significantly large, the opposite directions of the lateral forces exerted on the tip in the trace and retrace scanning processes could possibly lead to different behaviors of the cantilever, as intuitively speculated below. In the trace scanning process, the torque resulting from the lateral force exerted on the tip is produced in the same direction as the torque produced by the vertical force from the sample [Fig. 2(a)]. The torque produced by the lateral force decreases the slope near the end of the cantilever beam [Fig. 2(a)]. The amplitude measurement based on optical beam deflection sensing interprets this slope change as a reduction in the oscillation amplitude. The resulting amplitude signal is smaller than the case where only a vertical force acts on the tip; thus, the Z-scanner (and hence the sample) is displaced away from the tip by

feedback control [Fig. 2(a)]. In contrast, in the retrace scanning process, the torque resulting from the lateral force is produced in the direction opposite to the torque produced by the vertical force from the sample [Fig. 2(b)]. The lateral force increases the slope near the end of the cantilever beam [Fig. 2(b)], which is interpreted as rise in the oscillation amplitude. The resulting amplitude signal is larger than the case where only a vertical force acts on the tip from the sample; thus, the Z-scanner is displaced toward the tip by feedback control [Fig. 2(b)]. Although this Z-displacement reduces the error signal, both the lateral and vertical forces (as well as their resultant force) become larger.

To closely inspect the mechanism that produces the error difference between the trace and retrace scanning processes, we simultaneously recorded the cantilever deflection and error signals as well as the feedback controller output during imaging under the conditions used above [Figs. 2(c) and 2(e) and supplementary material, Fig. S1 shows these signals recorded during imaging at 6.7 fps]. Note that the values of f_c, tip-end radius, and tip cone angle moderately vary with the cantilever used. In the typical data recorded during retrace imaging of an actin filament [Fig. 2(c), third from the left], a positive peak error of ~0.55 V (i.e., $A - A_s \approx 0.83$ nm) first appeared at the time indicated by arrow-1. This error then became approximately zero or slightly negative during ~15 cycles of cantilever oscillation. As the feedback bandwidth of our system including the cantilever is 30–40 kHz, the feedback control does not work within a single cycle of cantilever oscillation. Therefore, the quick error reduction immediately after the positive error peak must be caused mainly by tip–sample interactions. Immediately after this period of ~15 oscillation cycles, a negative peak error of ~-0.7 V (i.e., $A - A_s \approx -1.05$ nm) suddenly appeared at the time indicated by arrow-2. The positive error at arrow-1 suggests that the tip was pushed laterally at the rightmost sample edge. This lateral force resulted in a downward bending of the cantilever beam hence in an increased amplitude signal. In the next ~15 oscillation cycles corresponding to ~38 μs and an X-displacement of ~4 nm, the tip was pushed both vertically and laterally from the sample. Note that because of the tip size effect, the ~4 nm displacement does not imply that the tip end was brought by this X-displacement to the uppermost position of the actin filament with the radius of ~4 nm. The upward deflection caused by the vertical force was largely canceled by the downward deflection caused by the lateral force. Therefore, during this period, feedback Z-scanning was performed only in a small extent (see the green line) despite a strong resultant force from the vertical and lateral forces acting on the sample. The negative peak error at arrow-2 suggests that the lateral force exerted on the tip by this time was largely removed, resulting in the sudden appearance of a large amplitude reduction caused by the strong vertical force. In fact, the deflection signal on the bottom-half side was largely reduced around the time point of arrow-2. At and after this time point, no large lateral force acted on the tip; therefore, the feedback control operated properly. In other records of error signals during retrace imaging of actin filaments, the positive and negative peak errors at the time points of arrow-1 and arrow-2 and the error level between these time points varied in a moderate range (see supplementary material, Fig. S1). However, the positive and negative peak errors appeared consistently in this order, and the time interval between the peaks remained almost constant for a given cantilever tip. In the cases of trace imaging of an actin filament and a MT, the error
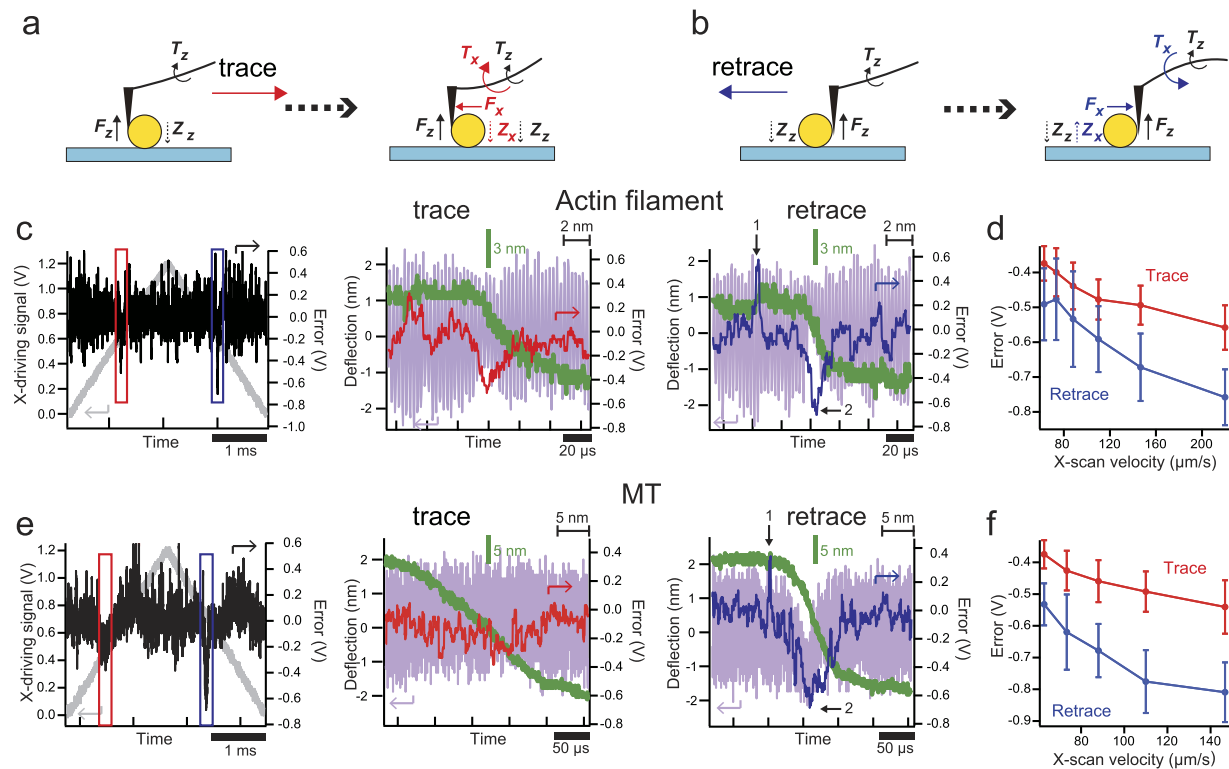
FIG. 2. Feedback error, deflection, and feedback control signals recorded during trace and retrace imaging at 5 fps. [(a) and (b)] Schematics showing torques T_x and T_z caused by lateral and vertical forces F_x and F_z, respectively, exerted on the tip from the sample during trace (a) and retrace (b) imaging in sample edge regions. The arrows denoted by Z_x and Z_z indicate the directions in which the Z-scanner is displaced to minimize errors caused by F_x and F_z, respectively. [(c) and (e)] Feedback error (red, blue), deflection (purple), and feedback control (green) signals recorded during trace and retrace imaging of actin filament (c) and MT (e); left: error signal in the entire scan rage (red and blue rectangles indicate scanning in positive step height regions), middle: during trace imaging of the positive step height regions, and right: during retrace imaging of the positive step height regions. [(d) and (f)] Dependence of negative peak error (mean ± s.d.; $n = 30$ for each plot) on X-scan velocity measured for actin filaments (d) and MTs (f).

signals were smaller than those in the retrace imaging and did not show clear responses indicative of lateral force effects [Figs. 2(c) and 2(e), second from the left].

Furthermore, retrace imaging of the positive step height region of a MT showed positive and negative peak errors in this order, while the interval between the peaks was longer, i.e., ~57 μs, corresponding to an X-scanner displacement of ~6.3 nm [Fig. 2(e), third from the left], due to the larger diameter of the MT. However, in the time region between the two error peaks, the error gradually became negative, which was remarkably caused by a gradual decrease in deflection on the upper-half side. After this period, the deflection on the upper-half side gradually recovered, while that on the bottom-half side gradually decreased. Then, the deflection on both sides gradually recovered, resulting in a smaller error approaching approximately zero. These behaviors of the error and deflection signals can be interpreted as follows [see Fig. 3(a)]. Around the time of the negative error peak [Fig. 3, (ii)], the tip is largely inclined inward by a strong lateral force from the sample. By this inclination, the vertical oscillations of the tip are accompanied by lateral vibrations (in the X-direction). However, the outward displacement in the X-direction is hampered by the sample, and hence, the upward deflection is also

hampered [see Fig. 3(a), top, (ii)], resulting in the suppression of cantilever deflection on the upper-half side. In contrast, the inward displacement in the X-direction is not hampered by the sample, and therefore, the downward deflection is not suppressed. In addition, the inward inclination of the tip is accompanied by downward bending of the cantilever beam at its end region, which increases the deflection signal on the bottom-half side. These interpretations are consistent with the observed deflection signals [Fig. 3(b), (ii)]. After the time of the negative error peak, the tip gradually makes contact with the sample at the tip-end region, while the side contact gradually diminishes. Therefore, the suppressed deflection on the upper-half side gradually recovers, while the deflection on the bottom-half side reduces gradually [see Fig. 3(a), (iii)], consistent with the observed deflection signal [Fig. 3(b), (iii)].

Next, glutaraldehyde-treated actin filaments and MTs running nearly along the Y axis were imaged at different X-scan velocities, during which the cantilever deflection and error signals were recorded. Figures 2(d) and 2(f) show the negative peak errors (mean ± s.d.) appearing during the trace and retrace imaging of the actin filaments [Fig. 2(d)] and MTs [Fig. 2(f)] at the respective X-scan velocities. Note that data were collected only for the cases in which

a
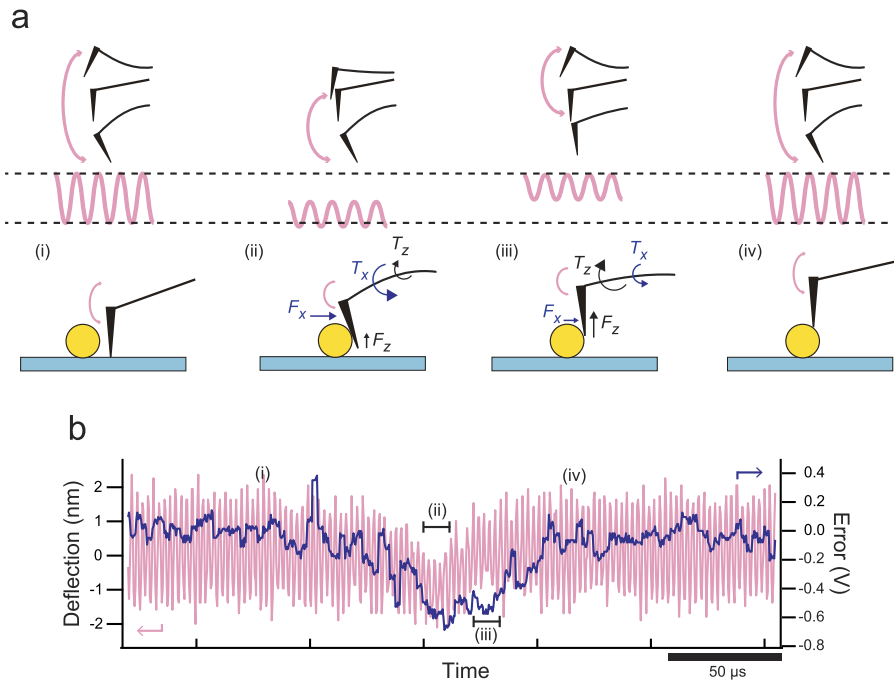
FIG. 3. Interpretation of error and deflection signals that appeared during retrace imaging of MT. (a) Cantilever oscillation and deflection depending on the lateral force exerted on the tip; top: schematics for cantilever oscillations in the respective time domains (i–iv) shown in (b), middle: deflection patterns in the respective time domains, and bottom: schematics showing cantilever deflection and tip inclination in the respective time domains. (b) Time domain classification by features of error and deflection signals [identical to those shown in Fig. 2(e), third from the left].

the glutaraldehyde-treated samples were not broken during imaging. The error difference between the trace and retrace imaging processes increased with increasing X-scan velocity. In addition, for different X-scan velocities and the trace and retrace scanning processes, the respective errors were almost identical between the two samples, despite their height difference of ~3-times. The error ratio (actin vs MT) was 0.95:1 for trace imaging and 0.82:1 for retrace imaging, on average. When lateral force effects are not considered, the maximum feedback control error ε_{max} can be theoretically expressed as $\varepsilon_{max} = h_0 \times \sin(\pi V_x \tau_0/\lambda)$, where τ_0 and $1/\lambda$ represent the delay time in the closed feedback loop and the spatial frequency of the tip-detected sample surface topography, respectively.[21] When the value of $\pi V_x \tau_0/\lambda$ is smaller than ~$\pi/4$, the maximum error becomes approximately proportional to h_0/λ. Similar values of h_0/λ for the two samples in their positive step height regions were confirmed by calculating the spatial frequencies for the simulated surface topographies of the samples (supplementary material, Note S1 and Figs. S2 and S3). From the error similarity between the two samples observed in retrace imaging, the influence of lateral forces on the negative peak error is also likely to be approximately proportional to h_0/λ. However, this issue requires further investigation. When a custom-made cantilever with $f_c \approx 1$ MHz in water was used for imaging of actin filaments, the error was reduced by 30%–40% (supplementary material, Fig. S4: dotted lines). This improvement is due to an increased feedback bandwidth and a shorter tip-sample contact time.

B. New X-scanning mode

From the observed feedback error difference between the trace and retrace scanning processes, the elimination of imaging during backward (retrace) scanning enables less disturbance and hence

faster imaging. To achieve this "only trace imaging" (OTI) mode, a DC offset signal ($A_{os} < 0$) was added to the true amplitude signal (A) during backward scanning, and the resulting false amplitude signal was fed to the feedback controller [Fig. 4(a)]. This operation withdraws the sample stage completely from the cantilever tip during backward scanning, except for the small left- and right-edge regions of the scan area. Moreover, the OTI mode enables further faster imaging by reducing the backward scan period. To achieve this, we can use a quasi-sawtooth waveform for X-scanning. This waveform with a period T and amplitude X_0 is expressed as

$$\frac{X(t)}{X_0} = \frac{1}{\alpha T}t \quad (0 \le t \le \alpha T), \tag{1}$$

$$X(t)/X_0 = -\frac{1}{(1-\alpha)T}t + \frac{1}{(1-\alpha)}(\alpha T \le t \le T), \tag{2}$$

where α is $0.5 < \alpha < 1$. The Fourier series of this function is given by

$$X(t)/X_0 = \frac{1}{2} + \sum_{n=1}^{\infty}\left[\frac{-1 + \cos(2n\pi\alpha)}{2n^2\pi^2\alpha(1-\alpha)}\cos\left(n\frac{2\pi}{T}t\right)\right.$$
$$\left. + \frac{\sin(2n\pi\alpha)}{2n^2\pi^2\alpha(1-\alpha)}\sin\left(n\frac{2\pi}{T}t\right)\right]. \tag{3}$$

Because the vertices of $X(t)$ contain high-frequency components, driving the X-scanner with $X(t)$ would easily generate vibrations in the X-scanner. We rounded the vertices using the finite Fourier series containing the first nine terms, which approximated the quasi-sawtooth waveform for $\alpha = 0.8$, and even for $\alpha = 0.9$ [Fig. 4(b), top]. However, the bottom vertex position slightly shifted in the right and upward directions, whereas the top peak position slightly
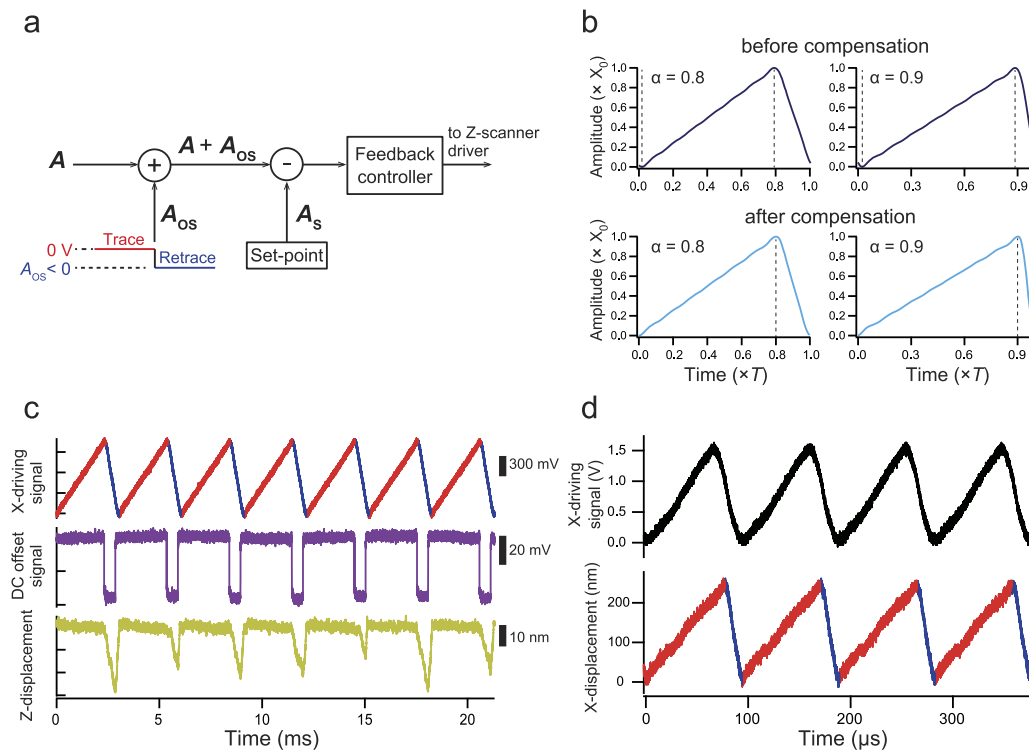
FIG. 4. Implementation of the OTI mode. (a) Circuit diagram for implementation of the OTI mode. (b) Wave forms constructed with finite Fourier series (containing the first nine terms) of quasi-sawtooth wave forms having $\alpha = 0.8$ and 0.9 (top) and those obtained after compensation for vertex position shifts caused by the finite Fourier series (bottom). (c) Driving signal for X-scanner (top), DC offset signal added to true amplitude signal (middle), and Z-scanner displacement (bottom). (d) Driving signal of 10.5 kHz for the X-scanner in the OTI mode after inverse compensation for vibrations (top) and measured displacement of X-scanner (bottom).

shifted in the left and downward directions. These shifts could easily be compensated for, as shown at the bottom of Fig. 4(b) and in supplementary material, Fig. S5. The compensation method is described in detail in supplementary material, Note S2. Figure 4(c) shows an X-scanner driving signal ($T = 3$ ms and $\alpha = 0.8$) constructed in this manner (top), together with the DC offset signal added to the true amplitude signal (middle) and the Z-scanner displacement (bottom). Our X-scanner with a resonant frequency of 47 kHz [supplementary material, Fig. S6(a)] and stroke range of 1.6 μm moved smoothly in the quasi-sawtooth waveform with $\alpha = 0.8$ [supplementary material, Fig. S6(b)], when driven at $f_x = 1.05$ kHz, corresponding to an imaging rate of 10 fps for the number of scan lines $N = 100$ (note that the time required for Y-scanning toward the origin of the scan area after one frame acquisition, $5/f_x$, is considered). Although the X-scanner exhibited vibrations when driven at 10.5 kHz (corresponding to 100 fps for $N = 100$) [supplementary material, Fig. S6(c)], the vibrations were completely suppressed using an inverse feedforward compensation method [Fig. 4(d) and supplementary material, Fig. S6(d)].[28,29]

C. Improved performances in "only trace imaging" (OTI) mode

To demonstrate the less disturbing/invasive and faster imaging capability of the OTI method, we first imaged an actin filament. Note that we hereafter used protein samples that were not treated

with glutaraldehyde. As shown at the top of Fig. 5(a) (Multimedia view), an actin filament oriented nearly along the Y axis could be imaged at 12.5 fps in the OTI mode, without disrupting the filament. In contrast, when the imaging mode was switched to the conventional scanning mode, the same actin filament was immediately broken under identical imaging conditions including the imaging rate [Fig. 5(a), bottom (Multimedia view)]. This clear difference is because of the elimination of retrace imaging in the OTI mode and, in part, because of the ~38% slower forward X-scan velocity in the OTI mode compared with that in the conventional mode under the same imaging rate. When "only retrace imaging" was conducted with a rounded quasi-sawtooth waveform having $\alpha = 0.8$, the actin filaments broke even at 10 fps (supplementary material, Fig. S7). The improved imaging capability of the OTI mode was further confirmed by imaging of a MT oriented nearly along the Y axis at 14.3 fps [Fig. 5(b), top (Multimedia view)]. In the conventional mode, the MT immediately broke at the same imaging rate [Fig. 5(b), bottom (Multimedia view)].

Next, we quantitatively evaluated the less disturbing/invasive and faster imaging capability of the OTI mode by measuring the non-breaking probability (P_{NB}) with which actin filaments and MTs could be imaged without breaking in a given time window (10 s). In this evaluation, the samples oriented nearly along the Y axis were imaged for an area of 200×100 nm^2 with 100×50 pixels at different X-scan velocities. We counted the number of imaging experiments that resulted in sample breakage (N_B) and those resulting in no
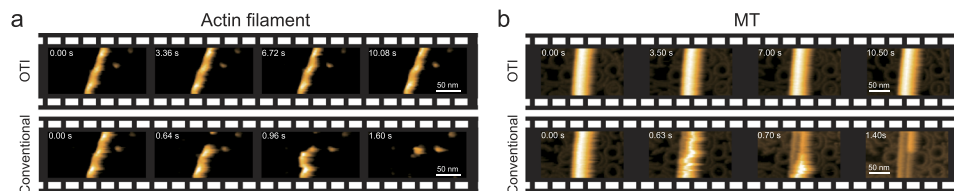
FIG. 5. Comparison of the OTI and conventional modes. (a) HS-AFM images of an actin filament captured at 12.5 fps in the OTI and conventional modes. (b) HS-AFM images of a MT captured at 14.3 fps in the OTI and conventional modes. Multimedia Views: https://doi.org/10.1063/5.0032948.1; https://doi.org/10.1063/5.0032948.2; https://doi.org/10.1063/5.0032948.3; https://doi.org/10.1063/5.0032948.4

sample breakage (N_{NB}), and we obtained P_{NB} as $P_{NB} = N_{NB}/(N_B + N_{NB})$. Figures 6(a) and 6(d) clearly show the faster scanning capability of the OTI mode. The X-scan velocity that produced $P_{NB} = 50\%$ was enhanced by the OTI mode from 179 to 240 μm/s (34% faster) for the actin filaments and from 205 to 299 μm/s (46% faster) for the MTs. As expected, the imaging rate that produced $P_{NB} = 50\%$ was more significantly improved by the OTI mode [Figs. 6(b) and 6(e)] from 8.2 to 16.4 fps for the actin filaments and from 9.3 to 22.4 fps for the MTs.

Subsequently, the amount of tip–sample interaction energy required to break actin filaments and MTs was quantitatively evaluated under the assumption that the energy lost from the oscillating cantilever by tip–sample contact is transferred to the sample. Because we could not measure the feedback control error at the time when these samples were broken, we estimated the error at a given X-scan velocity by extrapolation or interpolation from the relationships of the negative peak error vs X-scan velocity obtained for the trace and retrace imaging processes [Figs. 2(d) and 2(e)]. From the

Actin filament

MT
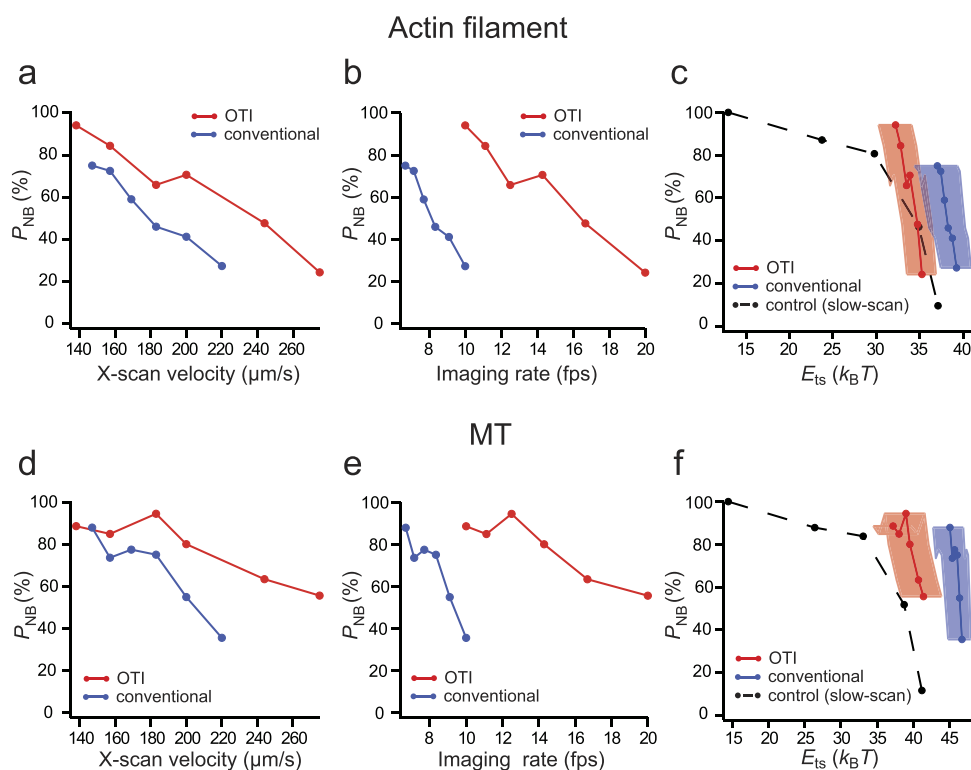
FIG. 6. Comparison of the OTI and conventional modes. Relationships of P_{NB} vs V_x [(a) and (d)], P_{NB} vs imaging rate [(b) and (e)], and P_{NB} vs E_{ts} [(c) and (f)] measured by imaging of the samples in the OTI and conventional modes. All measurements were repeated 27–52 times for each plot. The imaging conditions were as follows: imaging area = 200 nm × 100 nm; number of pixels = 100 × 50, A_f = 2.5 nm; and $A_s = 0.85 \times A_f$. The black broken lines in (c) and (f) represent the results obtained by imaging at 0.5 fps for 10 s using different set points. The measurements were repeated 21–32 times for each plot. The widths shown with the red and blue stripes in (c) and (f) present the standard deviations derived from those of the error signals at different X-scan velocities shown in Figs. 2(d) and 2(f).

error ε (<0) in nm, we estimated the tip–sample interaction energy E_{ts} as follows:[17,30]

$$E_{ts} = \gamma \times \frac{1}{2}k_c \times \left[A_f^2 - (A_s + \varepsilon)^2\right]/Q_c, \quad (4)$$

where γ (~0.9 for actin filaments and ~1.0 for MTs) is a correction factor for the amplitude reduction caused by a resonant frequency shift of the cantilever. We estimated the frequency shift from a phase shift measured using a fast phase detector[31] (supplementary material, Note S3). In this way, the relationships between P_{NB} and V_x [Figs. 6(a) and 6(d)] could be converted to those between P_{NB} and E_{ts}, as shown in Figs. 6(c) and 6(f). Here, the broken lines in Fig. 6(c) for the actin filaments and in Fig. 6(f) for the MTs indicate the P_{NB}–E_{ts} relationships obtained by control experiments where P_{NB} was measured by imaging at 0.5 fps with A_f = 2.5 nm and various values of A_s (0.45–0.85 × A_f). Note that the feedback control error is negligible at this low imaging rate. The data obtained in the control experiments indicated that the actin filaments and MTs were disrupted with E_{ts} values of ~35 and ~38 k_BT, respectively (k_B, Boltzmann constant; T = 298 K). The P_{NB}–E_{ts} relationships obtained from imaging in the OTI mode agreed approximately with those obtained from the control data, suggesting that the negative peak error is mostly caused by the vertical tip–sample interaction force and that the sample breakage is determined by the amount of energy lost from the oscillating cantilever by the tip–sample contact. Meanwhile, the P_{NB}–E_{ts} relationships obtained from imaging in the conventional imaging mode shifted toward higher energy by ~3.3 k_BT for the actin filaments and ~5 k_BT for the MTs, compared with the cases measured in the OTI mode. These shifts suggest that the negative peak error in retrace imaging does not precisely correspond to the energy required for sample breakage and that the samples might have been broken before the error reached the negative peak error.

D. Effectiveness of OTI mode

Finally, we demonstrated the effectiveness of the OTI mode by performing fast imaging of actin filaments and MTs oriented nearly along the X-direction and observing their polymerization processes that occur through weak protein–protein interactions. As shown in
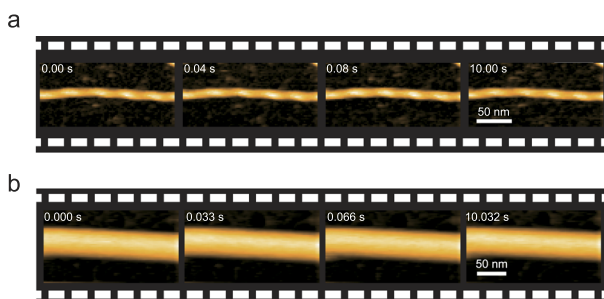
FIG. 7. Faster and less invasive imaging capability of the OTI mode. [(a) and (b)] HS-AFM images of an actin filament (a) and a MT (b) oriented nearly along the X-direction, captured in the OTI mode at 25 fps and 30 fps, respectively, with number of pixels = 100 × 50, A_f = 2.0 nm, and A_s = 1.7 nm. These imaging experiments were repeated 28 times for each sample to obtain the value of P_{NB} (>90%). Multimedia views: https://doi.org/10.1063/5.0032948.5; https://doi.org/10.1063/5.0032948.6

Figs. 7(a) and 7(b) (Multimedia view), the OTI mode enabled imaging of the actin filaments at 25 fps (n = 28) and the MTs at 30 fps (n = 28), without breaking them (P_{NB} > 90%). In the conventional imaging mode, the actin filaments and MTs oriented nearly along the X-direction were easily broken at these imaging rates (P_{NB} < 40% for actin filaments and P_{NB} < 60% for MTs; n = 24 for both samples). Thus, the OTI mode enhances the speed performance of HS-AFM ~2.5 times, indicating that trace imaging is further less disturbing/invasive than retrace imaging for protein samples with relatively small surface corrugations and low spatial frequencies.

To observe the polymerization processes of actin filaments, partially biotinylated actin filaments were attached onto the surface of two-dimensionally crystalized tamavidin 2-LPI, which has a strongly affinity for biotin. Unlabeled G-actin (actin monomers) was added to the solution (final concentration: 0.5 μM), without phalloidin. In the case of MTs, they were attached onto a bare mica surface, and tubulin dimers were added (final concentration: 0.5 μM), without
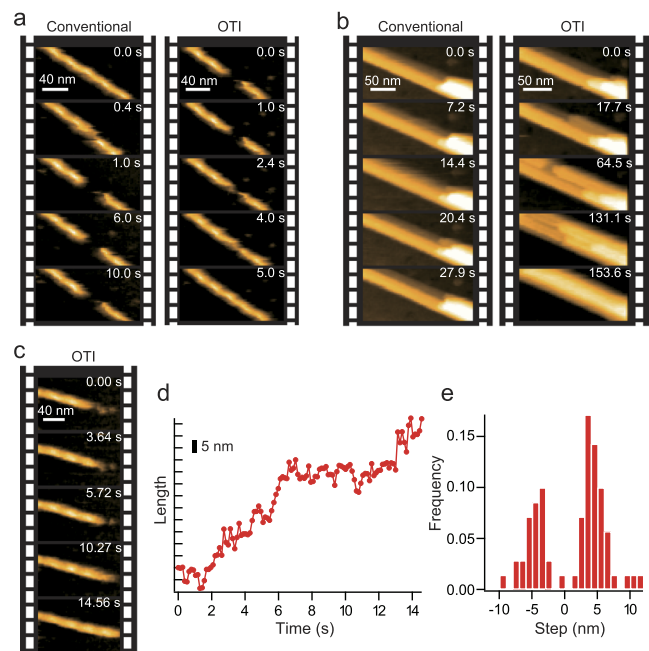
FIG. 8. Comparison of the OTI and conventional modes. (a) HS-AFM images showing breakage of an actin filament and subsequent polymerization from the broken filament ends in the presence of G-actin. Just before t = 2.4 s, A_s was changed from 1.3 to 1.9 nm (A_f = 2.2 nm), and imaging in the conventional mode was continued up to t = 10.8 s (left). Then, the imaging mode was switched to the OTI mode (right). (b) HS-AFM images showing tubulin polymerization from ends of protofilaments within a broken MT in the presence of tubulin dimers. After breakage of a MT under A_s = 1.5 nm (A_f = 2.5 nm), the broken MT was first imaged in the conventional mode at 3.3 fps with A_s = 2.1 nm (left). Then, the imaging mode was switched to the OTI mode (right). (c) HS-AFM images showing actin polymerization from one end of a broken actin filament in the presence of G-actin. The imaging was performed in the OTI mode at 7.7 fps, with A_f = 2.2 nm and A_s = 1.9 nm. (d) Time course of length change of the actin filament shown in (c). (e) Distribution of length change occurring during intervals of 0.13 s obtained from (d). Multimedia views: https://doi.org/10.1063/5.0032948.7; https://doi.org/10.1063/5.0032948.8; https://doi.org/10.1063/5.0032948.9; https://doi.org/10.1063/5.0032948.10; https://doi.org/10.1063/5.0032948.11

taxol. For the partial breakage of these polymers and the subsequent observation of polymerization processes at the polymer ends, the polymer samples oriented nearly in the diagonal direction were chosen. To break the polymers, they were imaged at 5 fps in the conventional imaging mode with the cantilever set point adjusted at ~1.3 nm (A_f = 2.2 nm). Then, the set point was readjusted to 1.9 nm. As shown in the left of Fig. 8(a) at 6.0 s and 10.0 s (Multimedia view), actin polymerization from the broken filament ends could not be observed in the conventional imaging mode even at 5 fps. This is because the tip disturbed the weak association of G-actin with the polymer ends: $K_d ≈ 0.1$ and 0.5 μM at the plus and minus ends, respectively.[32] In fact, when the imaging mode was switched to the OTI mode, asymmetric polymerization was observed at 5 fps [Fig. 8(a), right, 0–5 s) (Multimedia view)]. In a separate experiment, polymerization was observed at 7.7 fps in the OTI mode [Fig. 8(c) (Multimedia view)], where discreet elongation and shortening with a step size of ~5 nm were evident [Figs. 8(d) and 8(e)]. In the case of MTs, polymerization could not be observed in the conventional imaging mode, even at 3.3 fps [Fig. 8(b), left (Multimedia view)]. This is because the K_d value for the binding of tubulin dimers to the ends of a protofilament is large (K_d = 5.0 μM for tubulins from bovine brain),[33] and the association between α and β tubulins is weak (K_d = 0.8 μM for tubulins from bovine brain).[34] When the imaging mode was switched to the OTI mode, polymerization was observed at 3.3 fps [Fig. 8(b), right (Multimedia view)].

III. CONCLUSIONS

In this study, we first observed that the feedback control error is larger in retrace imaging than in trace imaging. Based on this finding, we developed the OTI mode. This mode allows for not only less disturbing/invasive imaging but also faster imaging. For samples with high spatial frequency, the highest possible imaging rate is doubled by the OTI mode. For samples with low spatial frequency, the imaging rate is improved by a factor of ~2.5, as demonstrated through the imaging of actin filaments and MTs oriented nearly along the X-direction at 25 and 30 fps, respectively. Even for dynamic actin polymerization processes that occur through weak protein–protein interactions, the OTI mode enables faster imaging at ~8 fps. In the current state, where even a 50% improvement in the speed performance of HS-AFM is very difficult, the alternative method developed in this study is highly advantageous. We expect that our simple and highly effective method will soon be installed in the existing and upcoming HS-AFM systems and will improve a wide range of HS-AFM imaging studies in biophysics and other fields.

IV. MATERIALS AND METHODS
A. HS-AFM system and imaging

We used a lab-built HS-AFM apparatus[1] with slight modifications for this study. Our HS-AFM system is equipped with a dynamic feedback controller that can automatically adjust the gain parameters during imaging so that tip parachuting is suppressed even under the condition of weak tip–sample contact.[9] Only a digital-to-analog convertor board (PCI3305, Interface, Japan) and an addition

circuit were newly added to the system to generate the DC offset signal and add the offset signal to the true amplitude signal of the oscillating cantilever, respectively. The voltage and duration of the DC offset signal were changed using a lab-developed software program in Igor Pro (Wave Metrics Inc., USA.) These parameters were adjusted according to the X-scan velocity. Commercially available cantilevers (AC10DS, Olympus, Japan) with a spring constant of ~0.1 N/m, resonance frequency of ~500 kHz in water, and quality factor of ~1.5 in water were used. An EBD tip was grown for 1.5 min on the original tip in an atmosphere of sublimated ferrocene vapor using a field emission scanning electron microscope (SUPRA40VP, Zeiss, Germany). The grown tip was sharpened by radiofrequency plasma etching for 1 min at 15 W in an argon environment using a plasma cleaner (Tergeo Plasma Cleaner, Pie Scientific, USA). In addition, custom-made cantilevers (BL-AC7DS-KU2, Olympus, Japan) with a spring constant of 0.15–0.2 N/m, resonance frequency of ~1 MHz in water, and quality factor of 2–3 in water were used to check the dependence of the feedback control error on the cantilever resonant frequency. The imaging conditions used, such as the number of scan lines and the values of A_f and A_s, are described in figure legends. Procedures for EBD tip preparation and HS-AFM imaging have been described in detail in a previous article.[35]

B. Preparation of protein samples

Actin was prepared from rabbit skeletal muscles as described previously.[36] Actin filaments were bound to an equimolar amount of phalloidin (Thermo Fisher, USA). For HS-AFM imaging of actin filaments, freshly cleaved mica was treated with 0.1% 3-aminopropyl triethoxysilane (Sigma Aldrich, USA) for 3 min, unless stated otherwise. After the surface was washed with pure water (200 μl), actin filaments (1 μM) were deposited on the surface and incubated for 10 min. After the surface was washed with F-Buffer containing 20 mM imidazole-HCl (pH 7.6), 50 mM KCl, 2 mM MgCl$_2$, and 1 mM EGTA, all measurements were performed in F-Buffer, unless stated otherwise. To measure the error signals (Figs. 1 and 2), the surface-attached actin filaments were treated with 0.1% glutaraldehyde for 15 min and then washed with F-Buffer. For the HS-AFM observation of actin polymerization (Fig. 8), actin filaments were formed from unlabeled G-actin and biotinylated G-actin at the molar ratio of 0.8:0.2 and then stabilized with an equimolar amount of phalloidin. Biotinylation of G-actin was performed in G-buffer containing 10 mM TES-KOH (pH 7.0), 0.2 mM CalCl$_2$, 0.1 mM NaN$_3$, and 0.2 mM ATP using a 5 M excess biotin-PEAC$_5$-maleimide (Dojindo, Japan). Then, the biotinylated G-actin was filtered with a centrifugal filter (Amicon Ultra, Millipore Corp., USA) to remove free biotin-PEAC$_5$-maleimide. The partially biotinylated actin filaments were placed on the surface of two-dimensional crystals of tamavidin two-LPI (Wako Chemicals, Japan) directly formed on a mica surface, as described previously.[37] Then, 0.5 μM G-actin, 0.2 mM ATP, and 1 mM DTT were added to the sample chamber solution containing an additional 50 mM KCl in F-buffer. MTs were prepared by the polymerization of porcine brain tubulin dimers (Cytoskeleton, Inc., USA). Tubulin proteins (1 mg/ml) were incubated with GTP (1 mM) for 15 min at 37 °C in PEM buffer containing 80 mM PIPES-NaOH (pH 6.9), 1 mM MgCl$_2$, and 1 mM

EGTA, followed by the addition of taxol (200 μM). After incubation for 15 min at 37 °C, the MTs were purified using a centrifugal filter (Amicon Ultra, Millipore Corp., USA). To measure the error signals (Figs. 1 and 2), glutaraldehyde (0.1%) was added to the MTs and incubated for 10 min before centrifugation. The MTs were then deposited onto freshly cleaved mica and incubated for 30 min. After the surface was washed with PEM buffer, all measurements were performed in PEM buffer. For the HS-AFM observation of tubulin polymerization from the ends of a broken MT (Figs. 8), 0.5 μM tubulin dimers and 100 μM GTP were added to the solution.

SUPPLEMENTARY MATERIAL

The following data are available as the supplementary material: captions for Supplementary Movies S1–S11; feedback control error, cantilever deflection, and feedback controller output signals recorded during retrace imaging of an actin filament and a MT at 6.7 fps; calculations of the spatial frequencies of tip-detected topographies of the modeled actin filament and MT; two-dimensional modeled tip shape and its contact with the X–Z cross-sections of modeled actin filament and MT oriented along the Y axis; calculations of tip-convoluted topographies of modeled actin filament and MT and their spatial frequencies; dependence of feedback control error on cantilever resonant frequency; detailed method of compensation for peak shifts in rounded quasi-sawtooth wave; quasi-sawtooth waves rounded by finite Fourier series containing the first nine terms; displacement of Z-scanner driven by rounded quasi-sawtooth wave and effect of inverse compensation on the displacement; detailed method to estimate the contribution of cantilever resonant frequency shift to amplitude reduction by tip–sample interactions; and comparison between "only trace imaging" and "only retrace imaging" modes for breakage of actin filaments.

Movie S1 shows the capability of the OTI mode to image an actin filament aligned along the Y axis at 12.5 fps without breakage; Movie S2, the breakage of an actin filament aligned along the Y axis during imaging in the conventional imaging mode at 12.5 fps; Movie S3, the capability of the OTI mode to image a MT aligned along the Y axis at 14.3 fps without breakage; Movie S4, the breakage of a MT aligned along the Y axis during imaging in the conventional imaging mode at 14.3 fps; Movie S5, the capability of the OTI mode to image actin filaments aligned along the X axis at 25 fps without breakage; Movie S6, the capability of the OTI mode to image MTs aligned along the X axis at 30 fps without breakage; Movie S7, the incapability of the conventional imaging mode to image actin polymerization at 5 fps; Movie S8, the capability of the OTI mode to image actin polymerization at 5 fps; Movie S9, the capability of the OTI mode to image the actin polymerization process at 7.7 fps; Movie S10, the incapability of the conventional imaging mode to image tubulin polymerization at 3.3 fps; and Movie S11, the capability of the OTI mode to image tubulin polymerization at 3.3 fps.

ACKNOWLEDGMENTS

DATA AVAILABILITY

The data that support the findings of this study are available within the article and its supplementary material. The source code for the OTI mode will be provided upon request.

REFERENCES

[1] T. Ando, T. Uchihashi, and T. Fukuma, "High-speed atomic force microscopy for nano-visualization of dynamic biomolecular processes," Prog. Surf. Sci. **83**, 337–437 (2008).

[2] T. E. Schäffer, J. P. Cleveland, F. Ohnesorge, D. A. Walters, and P. K. Hansma, "Studies of vibrating atomic force microscope cantilevers in liquid," Rev. Sci. Instrum. **80**, 3622–3627 (1996).

[3] T. Ando, N. Kodera, E. Takai, D. Maruyama, K. Saito, and A. Toda, "A high-speed atomic force microscope for studying biological macromolecules," Proc. Natl. Acad. Sci. U. S. A. **98**, 12468–12472 (2001).

[4] M. Kitazawa, K. Shiotani, and A. Toda, "Batch fabrication of sharpened silicon nitride tips," Jpn. J. Appl. Phys., Part 1 **42**, 4844–4847 (2003).

[5] M. B. Viani, T. E. Schäffer, G. T. Paloczi, L. I. Pietrasanta, B. L. Smith, J. B. Thompson, M. Richter, M. Rief, H. E. Gaub, K. W. Plaxco, A. N. Cleland, H. G. Hansma, and P. K. Hansma, "Fast imaging and fast force spectroscopy of single biopolymers with a new atomic force microscope designed for small cantilevers," Rev. Sci. Instrum. **70**, 4300–4303 (1999).

[6] T. Ando, N. Kodera, T. Uchihashi, A. Miyagi, R. Nakakita, H. Yamashita, and K. Matada, "High-speed AFM for studying the dynamic behavior of protein molecules at work," e-J. Surf. Sci. Nanotechnol. **3**, 384–392 (2005).

[7] G. Schitter, K. J. Astrom, B. E. DeMartini, P. J. Thurner, K. L. Turner, and P. K. Hansma, "Design and modeling of a high-speed AFM-scanner," IEEE Trans. Control Syst. Technol. **15**, 906–915 (2007).

[8] N. Kodera, H. Yamashita, and T. Ando, "Active damping of the scanner for high-speed atomic force microscopy," Rev. Sci. Instrum. **76**, 053708 (2005).

[9] N. Kodera, M. Sakashita, and T. Ando, "Dynamic proportional-integral-differential controller for high-speed atomic force microscopy," Rev. Sci. Instrum. **77**, 083704 (2006).

[10] N. Kodera, D. Yamamoto, R. Ishikawa, and T. Ando, "Video imaging of walking myosin V by high-speed atomic force microscopy," Nature **468**, 72–76 (2010).

[11] M. Yokokawa, C. Wada, T. Ando, N. Sakai, A. Yagi, S. H. Yoshimura, and K. Takeyasu, "Fast-scanning atomic force microscopy reveals the ATP/ADP-dependent conformational changes of GroEL," EMBO J. **25**, 4567–4576 (2006).

[12] T. Uchihashi, R. Iino, T. Ando, and H. Noji, "High-speed atomic force microscopy reveals rotary catalysis of rotorless F_1-ATPase," Science **333**, 755–758 (2011).

[13] T. Uchihashi, Y. Watanabe, Y. Nakazaki, T. Yamasaki, H. Watanabe, T. Maruno, K. Ishii, S. Uchiyama, C. Song, K. Murata, R. Iino, and T. Ando, "Dynamic structural states of ClpB involved in its disaggregation function," Nat. Commun. **9**, 2147 (2018).

[14] T. Watanabe-Nakayama, K. Ono, M. Itami, R. Takahashi, D. B. Teplow, and M. Yamada, "High-speed atomic force microscopy reveals structural dynamics of amyloid $\beta_{1\text{-}42}$ aggregates," Proc. Natl. Acad. Sci. U. S. A. **113**, 5835–5840 (2016).

[15] K. Matsuda, M. Sugawa, M. Yamagishi, N. Kodera, and J. Yajima, "Visualizing dynamic actin cross-linking processes driven by the actin-binding protein anillin," FEBS Lett. **594**(8), 1237–1247 (2020).

[16] J. Strasser, R. N. De Jong, F. J. Beurskens, J. Schuurman, P. W. H. I. Parren, P. Hinterdorfer, and J. Preiner, "Weak fragment crystallizable (Fc) domain interactions drive the dynamic assembly of IgG oligomers upon antigen recognition," ACS Nano **14**, 2739–2750 (2020).

[17] T. Ando, T. Uchihashi, and S. Scheuring, "Filming biomolecular processes by high-speed atomic force microscopy," Chem. Rev. **114**, 3120–3188 (2014).

[18] T. Uchihashi and S. Scheuring, "Applications of high-speed atomic force microscopy to real-time visualization of dynamic biomolecular processes," Biochim. Biophys. Acta, Gen. Subj. **1862**, 229–240 (2018).

[19] T. Ando, "High-speed atomic force microscopy," Curr. Opin. Chem. Biol. **51**, 105–112 (2019).

[20]G. R. Heath and S. Scheuring, "Advances in high-speed atomic force microscopy (HS-AFM) reveal dynamics of transmembrane channels and transporters," Curr. Opin. Struct. Biol. **57**, 93–102 (2019).

[21]T. Ando, T. Uchihashi, and N. Kodera, "High-speed AFM and applications to biomolecular systems," Annu. Rev. Biophys. **42**, 393–414 (2013).

[22]A. Miyagi, C. Chipot, M. Rangl, and S. Scheuring, "High-speed atomic force microscopy shows that annexin V stabilizes membranes on the second timescale," Nat. Nanotechnol. **11**, 783–790 (2016).

[23]N. Kodera, D. Noshiro, S. K. Dora, T. Mori, J. Habchi, D. Blocquel, A. Gruet, M. Dosnon, E. Salladini, C. Bignon, Y. Fujioka, T. Oda, N. N. Noda, M. Sato, M. Lotti, M. Mizuguchi, S. Longhi, and T. Ando, "Structural and dynamics analysis of intrinsically disordered proteins by high-speed atomic force microscopy," Nat. Nanotechnol. **16**, 181–189 (2021).

[24]A. P. Nievergelt, N. Banterle, S. H. Andany, P. Gönczy, and G. E. Fantner, "High-speed photothermal off-resonance atomic force microscopy reveals assembly routes of centriolar scaffold protein SAS-6," Nat. Nanotechnol. **13**, 696–701 (2018).

[25]A. Miyagi and S. Scheuring, "A novel phase-shift-based amplitude detector for a high-speed atomic force microscope," Rev. Sci. Instrum. **89**, 083704 (2018).

[26]T. Uchihashi, H. Watanabe, S. Fukuda, M. Shibata, and T. Ando, "Functional extension of high-speed atomic force microscopy," Ultramicroscopy **160**, 182–196 (2016).

[27]C. Yang, J. Yan, M. Dukic, N. Hosseini, J. Zhao, and G. E. Fantner, "Design of a high-bandwidth tripod scanner for high speed atomic force microscopy," Scanning **38**, 889–900 (2016).

[28]G. Schitter and A. Stemmer, "Identification and open-loop tracking control of a piezoelectric tube scanner for high-speed scanning-probe microscopy," IEEE Trans. Control Syst. Technol. **12**(3), 449–454 (2004).

[29]Y. Li and J. Bechhoefer, "Feedforward control of a closed-loop piezoelectric translation stage for atomic force microscope," Rev. Sci. Instrum. **78**, 013702 (2007).

[30]T. R. Rodriguez and R. Garcia, "Theory of Q control in atomic force microscopy," Appl. Phys. Lett. **82**, 4821 (2003).

[31]T. Uchihashi, T. Ando, and H. Yamashita, "Fast phase imaging in liquids using a rapid scan atomic force microscope," Appl. Phys. Lett. **89**, 213112 (2006).

[32]M.-F. Carlier and D. Pantaloni, "Review article: Control of actin dynamics in cell motility," J. Mol. Biol. **269**, 459–467 (1997).

[33]A. Davis, C. R. Sage, L. Wilson, and K. W. Farrell, "Purification and biochemical characterization of tubulin from the budding yeast *Saccharomyces cerevisiae*," Biochemistry **32**, 8823–8835 (1993).

[34]J. Howard, Mechanics of Motor Proteins and the Cytoskeleton (Sinauer Associates, Sunderland Massachusetts, 2001).

[35]T. Uchihashi, N. Kodera, and T. Ando, "Guide to video recording of structure dynamics and dynamic processes of proteins by high-speed atomic force microscopy," Nat. Protoc. **7**, 1193–1206 (2012).

[36]T. Sakamoto, I. Amitani, E. Yokota, and T. Ando, "Direct observation of processive movement by individual myosin V molecules," Biochem. Biophys. Res. Commun. **272**, 586–590 (2000).

[37]D. Noshiro and T. Ando, "Substrate protein dependence of GroEL-GroES interaction cycle revealed by high-speed AFM imaging," Philos. Trans. R. Soc., B **373**, 20170180 (2018).